GDCh

Research Articles

Angewandte
Chemie
International Edition
www.angewandte.org

VIP | **Li-Ion Batteries** | *Very Important Paper*

One-Step Calcination Synthesis of Bulk-Doped Surface-Modified Ni-Rich Cathodes with Superlattice for Long-Cycling Li-Ion Batteries

Yongjiang Sun[+], Changhong Wang[+], Wenjin Huang, Genfu Zhao, Lingyan Duan, Qing Liu, Shimin Wang, Adam Fraser, Hong Guo,* and Xueliang Sun*

Abstract: Nickel-rich (Ni $\geq$ 90 %) layered cathodes are critical materials for achieving higher-energy-density and lower-cost next-generation Li-ion batteries (LIBs). However, their bulk and interface structural instabilities significantly impair their electrochemical performance, thus hindering their widespread adoption in commercial LIBs. Exploiting Ti and Mo diffusion chemistry, we report one-step calcination to synthesize bulk-to-surface modified $LiNi_{0.9}Co_{0.09}Mo_{0.01}O_2$ (NCMo90) featuring a 5 nm Li_2TiO_3 coating on the surface, a Mo-rich Li^+/Ni^{2+} superlattice at the sub-surface, and Ti-doping in the bulk. Such a multi-functional structure effectively maintains its structural integrity upon cycling. As a result, such NCMo90 exhibits a high initial capacity of 221 mAh g^{-1} at 0.1 C, excellent rate performance (184 mAh g^{-1} at 5 C), and high capacity retention of 94.0 % after 500 cycles. This work opens a new avenue to developing industry-applicable Ni-rich cathodes for next-generation LIBs.

Introduction

Electric vehicles (EVs) primarily powered by Li-ion batteries (LIBs) have gained popularity in recent years due to their environmental and economic benefits.[1–3] To develop more efficient, powerful, and longer-lasting EVs, advanced LIBs with higher energy density and lower cost are highly desired. As a critical material that determines the accessible energy density and cost of LIBs, a nickel (Ni)-rich layered cathode material with a Ni content of over 90 % has received intense interest from academia and industry because of its high specific capacity of over 200 mAh g^{-1} and lower cost than traditional $LiCoO_2$ and $Li[Ni_{0.9}Co_xMn_y/Al_y]O_2$.[4,5] However, the application of Ni-rich layered cathodes in LIBs suffers from poor cycling stability, which can be explained by three main phenomena. **(1) Surface reconstruction**, when the LIB is charged to high voltage, Ni-rich layered cathode generally undergoes a phase reconstruction from layered to spinel to rock salt structure accompanied by lattice oxygen loss, especially at the surface.[6] The surface structural reconstruction considerably impedes interfacial ion transport, thus increasing internal resistance and decreasing cycling stability.[7] **(2) Transitional metal dissolution**, where the transitional metals readily dissolve into the electrolyte, then migrate to the anode surface and poison the interfacial solid electrolyte interphase (SEI), thus deteriorating cycling stability.[8] **(3) Intergranular cracking**, where the inhomogeneous internal strain generated during the lithiation and delithiation processes leads to intergranular cracking,[9–11] further increasing transition metal dissolution and exaggerating the surface reactivity with electrolytes.[12,13] Together, these three phenomena jointly lead to the fast capacity fading of Ni-rich cathodes.

Most recently, diverse strategies have been proposed to address these issues, such as elemental doping,[14–21] surface coating,[22–26] and morphology engineering.[27–31] Among these strategies, doping with high-valency elements (such as Ta^{5+}, Mo^{6+} or W^{6+}) to form Li^+/Ni^{2+} superlattices and radially-oriented long grains has been proven effective.[32–36] The Li^+/Ni^{2+} superlattice structure effectively prevents the collapse of the Li–O slabs in the deeply delithiated state, while the radially oriented grain geometry can effectively dissipate strain accumulation, thus suppressing intergranular cracking. Therefore, high-valency element-doped Ni-rich cathodes ($LiNi_{0.9}Co_{0.09}M_{0.01}O_2$, where M=$Ta^{5+}$, Mo^{6+} or W^{6+}) with a sub-surface Li/TM cation-ordered superlattice have been regarded as the most promising for deployment in the next-generation LIBs to realize higher energy density and lower cost. However, several interesting scientific questions have not been addressed yet regarding this emerging Ni-rich cathode. **First**, considering that all the high-valency elemental dopants in Ni-rich cathodes are introduced using a solid-state sintering process, is it possible to introduce the dopants instead during the coprecipitation process? **Second**, can the cycling stability of high-valency element-doped Ni-rich

[*] Y. Sun,[+] W. Huang, G. Zhao, L. Duan, Q. Liu, S. Wang, H. Guo
International Joint Research Center for Advanced Energy Materials of Yunnan Province, Electron Microscope Center of Yunnan University, School of Materials and Energy, Yunnan University 650091 Kunming (China)
E-mail: guohong@ynu.edu.cn

C. Wang,[+] A. Fraser, X. Sun
Department of Mechanical and Materials Engineering, University of Western Ontario
1151 Richmond St., N6A3K7 London, Ontario, (Canada)
E-mail: xsun9@uwo.ca

[+] These authors contributed equally to this work.

cathodes with a sub-surface superlattice be further improved by surface coating and bulk doping? If yes, what strategies can realize this structure, and is there a one-step strategy that could obtain these structural features simultaneously?

In this work, we report bulk-doped and surface-modified $LiNi_{0.9}Co_{0.09}Mo_{0.01}O_2$ (NCMo90) cathode with a sub-surface superlattice using first-of-its-kind coprecipitation followed by one-step calcination. High-valency molybdenum (Mo^{6+}) is introduced to synthesize NCMo90 precursor during the coprecipitation process. $Ti(OH)_4$ surface coating is added to the NCMo90 precursor surface using a facile sol-gel process. Exploiting different migration energy barriers of Mo and Ti in the layered oxide lattice, a Ti-doped bulk, Mo-rich Li^+/Ni^{2+} cation-ordered subsurface superlattice, and a nano-scale Li_2TiO_3 surface coating in NCMo90 is simultaneously formed in one-step calcination. As illustrated in Scheme 1, the nanoscale Li_2TiO_3 surface modification effectively prevents electrolyte decomposition, hydrogen fluoride (HF) attack, and transition metal dissolution. At the same time, the sub-surface Mo-rich superlattice and Ti-doping in bulk maintain structural stability from the bulk to the surface during the cycling. Therefore, this NCMo90 with multi-functional structural features demonstrates high discharge capacity, good rate performance, and long cycling stability. This work provides a facile synthesis strategy for designing bulk-to-surface modified Ni-rich layered cathodes, which lays the groundwork for developing next-generation LIBs with lower cost, higher energy density, and longer lifespan.

Results and Discussion

At first, density functional theory (DFT) calculation was performed to evaluate the structural energy of $LiNiO_2$ doped by Ti or Mo in different layers (Figures 1a and 1b, Figure S1). $LiNiO_2$ was chosen as a structural base to simplify as it has a similar structure and electrochemical property with NCMo90 (Figure S1).[7,11,37,38] Ti-doping in the second and third transition metal (TM) layers show relatively lower energy than in the first layer (Figure 1c). On the contrary, the structure with Mo in the first TM layer has lower energy than those in the second and third TM layers. In terms of kinetics, the migration energy barrier of Ti in bulk is lower than that of Mo, indicating Ti easily diffuses into the bulk while Mo is likely to concentrate at the surface due to the slow diffusion kinetics. Furthermore, the migration energy barrier of Mo becomes higher after Ti doping (Figure 1d), further suggesting that Mo tends to concentrate at the surface and sub-surface after Ti doping. The different diffusivity of Ti and Mo in the layered cathode eventually forms a unique NCMo90 featuring a Mo-rich surface and Ti-doped bulk.

In addition, the charge differences of bare and Ti-modified cathode were calculated to investigate the influence of Ti on the structure (Figures S1a–c), demonstrating that Ti and O interact more strongly than Ni or Co do.[26,38] The stronger Ti–O bond can effectively suppress the structural transition from H2 to H3 during charge/discharge.[14] Furthermore, the electronic density of states (DOS) was analyzed to understand the electronic conductivity change, which can be reflected by the electronic DOS
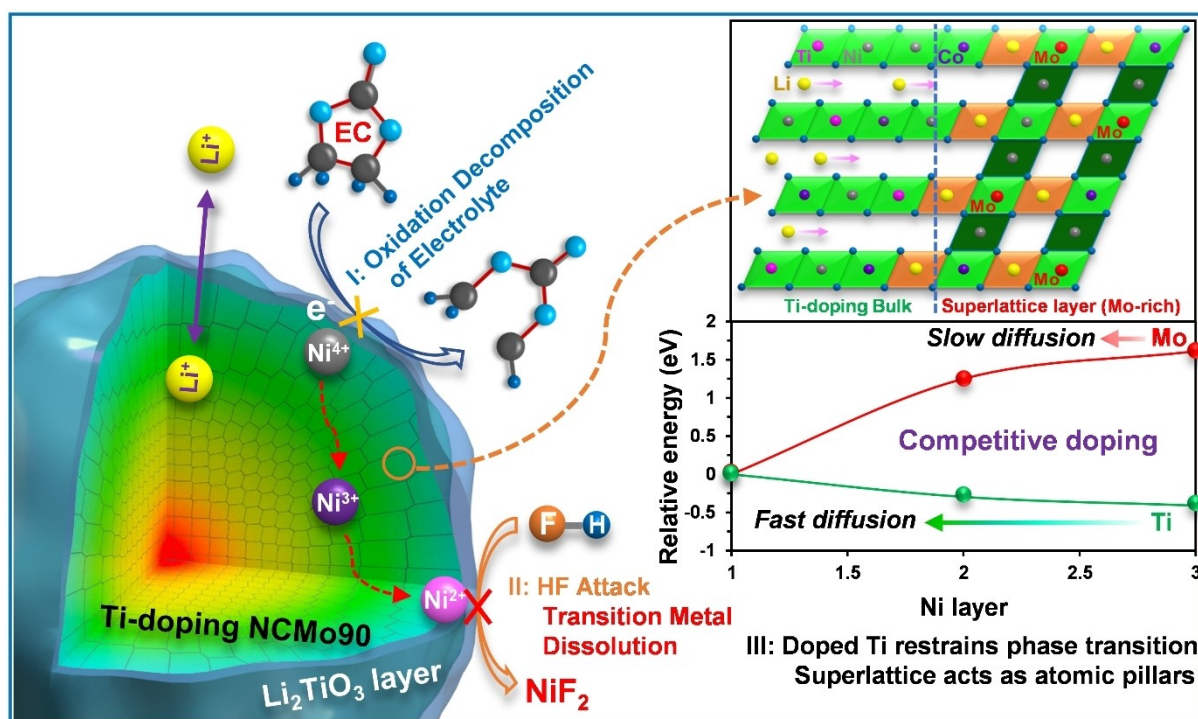
Scheme 1. Schematic illustration of the structural design concept for bulk-to-surface modified $LiNi_{0.9}Co_{0.09}Mo_{0.01}O_2$ cathode.
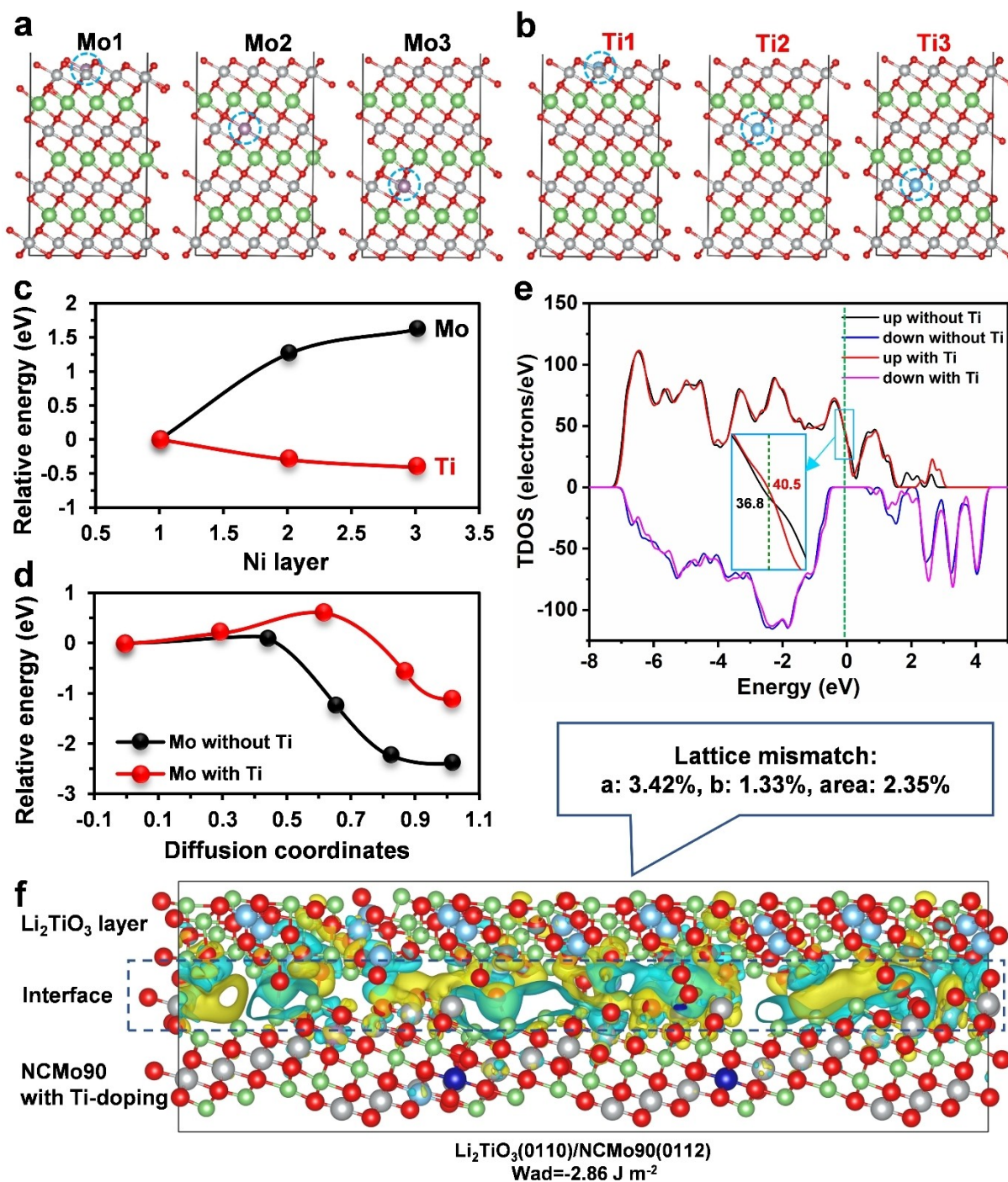
Figure 1. DFT calculations of the roadmap for Ti-modified NCMo90. a) Doping Mo and b) Ti to the 1st, 2nd, and 3rd Ni-rich layers, respectively. c) The energy of different structures with doping Ti and Mo to the 1st, 2nd, and 3rd Ni-rich layers. d) Mo migration energy barrier from the surface to the first layer with and without Ti. e) The total density of states plots of pristine and Ti-modified NCMo90. f) The charge density difference of the Li_2TiO_3/NCMo90 interface.

near the Fermi level.[25,26] After Ti modification, the introduced 2p state of Ti increases the electronic DOS near the Fermi level (Figure 1e, Figure S1d and S1e), indicating that Ti-doing can boost the electronic conductivity of NCMo90.[26] Thus, Ti doping in NCMo90 can improve structural stability and bolster electronic conductivity, which is expected to enhance its electrochemical cycling stability

and rate performance. Apart from Ti doping, a Li_2TiO_3 layer can form on the cathode surface because of the reaction between Ti and $LiOH \cdot H_2O$.[39,40] Thus, DFT calculations were conducted to gain more insight into the interface between the Li_2TiO_3 coating layer and NCMo90 (Figure 1f). The lattice mismatch between Li_2TiO_3 (0110) and NCMo90 (0112) is less than 10 % (a: 3.42 %, b: 1.33 %, area: 2.35 %),

implying their interfacial lattice is well matched. In addition, the low interfacial work of adhesion (W_{ad}) of $-2.86\,J\,m^{-2}$ further suggests a strong interfacial interaction between the Li_2TiO_3 (0110) and NCMo90 (0112) planes. Moreover, considering that Li_2TiO_3 has a three three-dimensional Li^+-transport pathway, wide electrochemical stability window, and desirable structural stability, the Li_2TiO_2 coating layer on NCMo90 not only facilitates Li^+ migration across the interface but also reduces the erosion of cathodes by electrolytes, which could stabilize the electrochemical performance of the cathode.[41–43]

The NCMo90 hydroxide precursor has a homogeneous morphology with an average particle diameter of about 8 µm (Figure S2a). Each precursor secondary particle comprises densely-packed numerous thin plate-like primary grains. Inductively coupled plasma-optical emission spectroscopy (ICP-OES) analysis illustrates that the proportion of Ni, Co, and Mo in the precursor is 0.9023, 0.0892, and 0.0095, respectively. After the $Ti(OH)_4$ sol-gel process, the surface is uniformly covered by a flocculent layer while its monodispersity and average particle size do not change (Figure S2b). The X-ray diffraction (XRD) analysis in Figure S3 confirms that the precursors match well with β-$Ni(OH)_2$.[44] The absence of $Ti(OH)_4$ diffraction peaks implies that the surface coating is amorphous. The energy-dispersive spectroscopy (EDS) mapping further illustrates that all the elements are uniformly distributed (Figure S4).

After one-step calcination at 730 °C for 10 hours, the structural phase changes to an α-$NaFeO_2$ structure (JCPDS No. 09-0063) (Figure S5),[45] suggesting the bare and Ti-modified cathodes were successfully obtained with high crystallinity. Both the lattice parameters (*a*, *c*) and volume (*V*) gradually increase with Ti contents (Table S1), implying Ti doping into the lattice can increase the height of Li–O slab (h_{Li-O}),[46] which is beneficial for Li^+ transport kinetics. However, excess Ti-doping leads to more disordered cation mixing, which hinders Li^+ migration and decreases discharge capacity. Overall, 1.0 mol % Ti-modified NCMo90 possesses the largest Li–O slab (h_{TM-O}) height, the strongest Ti–O chemical bond, and the lowest degree of cation mixing, thus expected to show optimal electrochemical performance.

The chemical components of all samples were confirmed by ICP-OES (Table S2), which matches very well with their stoichiometric ratio. High-resolution XPS was further performed to verify the chemical valence states. Both pristine and 1 mol % Ti-modified NCMo90 present the feature peaks of Ni, Co, and Mo, but the Ti peak is only detected in 1 mol % Ti-modified NCMo90 (Figure S6). Co^{3+} and Mo^{6+} are identified in both samples (Figures S7a and S7b), indicating that Ti modification does not change the valence state of Mo and Co. Ni^{2+} and Ni^{3+} co-exist in the Ni spectra (Figure S7c). However, pristine NCMo90 possesses fewer Ni^{2+} (19.1 %) than the Ti-modified NCMo90 (20.8 %), implying a slightly greater Li^+/Ni^{2+} mixing in the latter. This result is consistent with the XRD refinement results mentioned above. Regarding Ti (Figure S7d), the modified NCMo90 exhibits two peaks at 457.78 eV and 463.50 eV,

which is characteristic of Ti^{4+} according to previous reports.[40,43]

The morphology of cathodes was examined by scanning electron microscopy (SEM). The pristine spherical secondary particles comprise many nanoscale primary grains (Figure 2a). The 1.0 wt % Ti-modified NCMo90 has similar morphology and grain sizes as the pristine sample (Figure 2b). The EDS mapping of Ti-modified NCMo90 also shows homogeneous Ti distribution in NCMo90 (Figure S8). Transmission electron microscopy (TEM) was further performed to identify the surface coating. A 5 nm uniform coating layer is generated on the NCMo90 surface (Figure 2c). Notably, the interplanar spacing of the coating layer is 0.206 nm, which is characteristic of ($\bar{1}$33) plane of Li_2TiO_3,[47] suggesting the ion-conductive Li_2TiO_3 coating is successfully established on the NCMo90 surface.

Furthermore, the lattice structure of NCMo90 was examined by atomic-resolution TEM. An ordered super-lattice structure at the sub-surface and a typical layered structure in the bulk are observed and further confirmed by their Fast Fourier Transform (FFT) patterns (Figure 2d and Figure S9a).[35] As previously mentioned,[36,48] the super-lattice structure originates from the high-valency metal elemental doping. Here, Mo^{6+} facilitates partial reduction of Ni^{3+} to Ni^{2+} to maintain charge balance, which leads to the partial migration of Ni^{2+} into Li–O slabs and the equal migration of Li^+ into TM–O layer, thus forming ordered Li^+/Ni^+ superlattice. Compared to the disordered Li^+/Ni^{2+} mixing, the ordered Li^+/Ni^{2+} superlattice possess lower delithiation energy and can stabilize the delithiated structure, thus improving cycling stability.[36] It is worth noting that the unique ordered superlattice structure remains after Ti-modification, according to the HAADF image (Figure 2e) and FFT patterns (Figure S9b), which illustrates that Ti-modification can maintain the superlattice structure resulting from the ordered Li^+/Ni^{2+} anti-site defects. It is noted that Mo is mainly concentrated at the surface instead of diffusing into the bulk (Figure S10), which is fully consistent with Mo diffusivity in $LiNiO_2$ bulk, as confirmed by DFT calculation in Figures 1c and d.

Moreover, the interplanar spacing of the (003) plane of 1.0 mol % Ti-modified NCMo90 is 0.4850 nm, larger than that of pristine NCMo90 (0.4719 nm) (Figure S11). As discussed in the part of DFT calculations, the chemical Ti–O bonding is stronger than Ni–O bonding,[26,38] which leads to higher charge density for O atoms, increasing the electrostatic repulsion between oxygen layers. Consequently, the heights of Li–O slabs (h_{Li-O}) gradually increase with Ti doping, which is also consistent with the TEM results (Figure S11). This enlarged spacing is beneficial to the migration of Li ions.[45,46] Interestingly, a lattice distortion is observed in Ti-modified NCMo90 (Figure 2e; marked with a red rectangle), which may result from the enlarged spacing of the (003) plane. The elemental mapping obtained by STEM further verifies the homogeneous distribution of Ni, Co, Ti and O in two samples (Figure S12).

In summary, comprehensive structural analyses show that pristine NCMo90 has a feature of Mo-rich Li^+/Ni^{2+} superlattice at the sub-surface, while 1 mol % Ti-modified
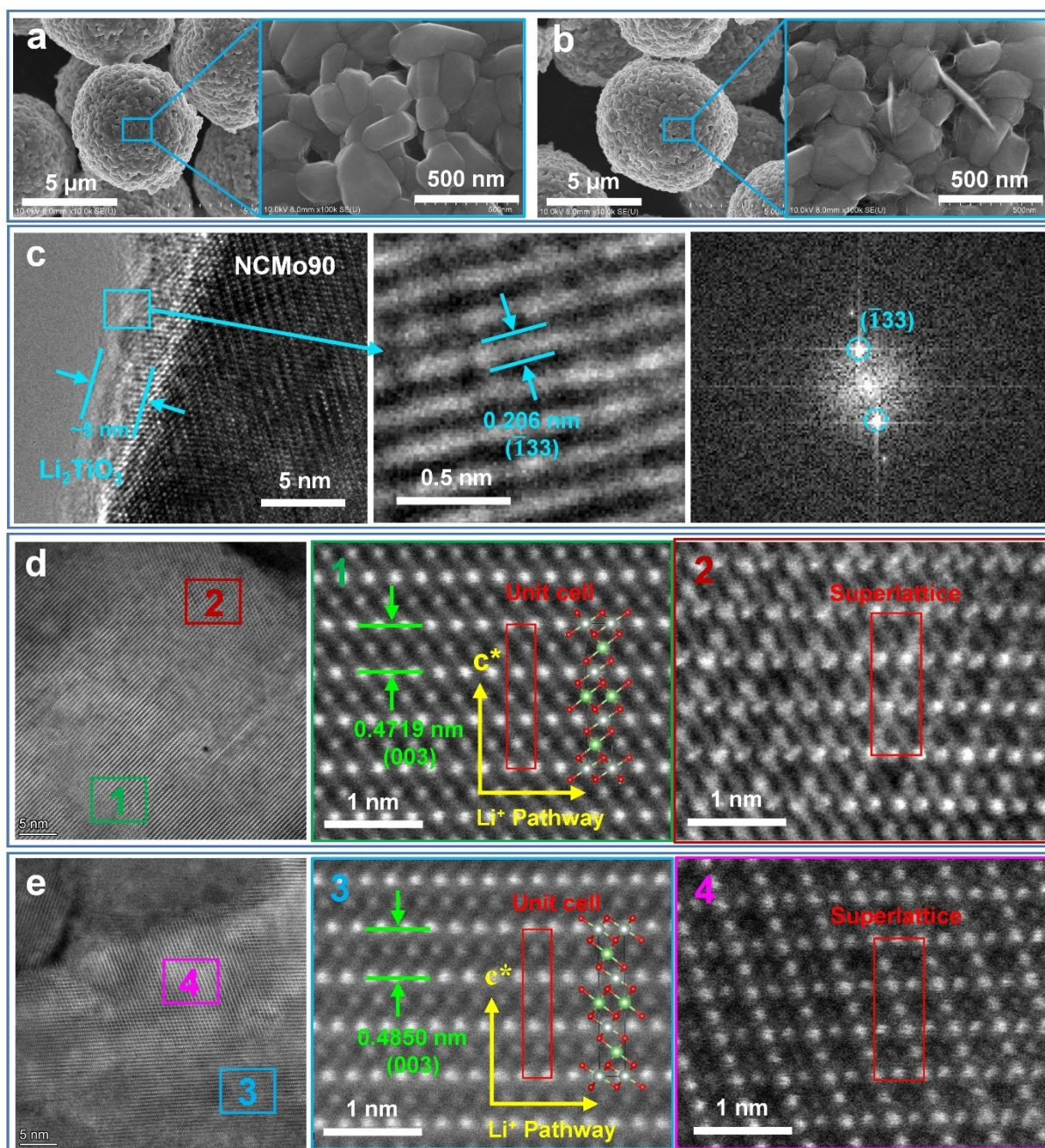
Figure 2. SEM images of pristine (a) and 1.0 mol% Ti-modified NCMo90 (b). c) HAADF-STEM image of Li_2TiO_3 coating layer and NCMo90 as well as the corresponding FFT of Li_2TiO_3 coating layer. HAADF-STEM images of pristine (d) and 1.0 mol% Ti-modified NCMo90 (e).

NCMo90 not only maintains the Mo-rich Li^+/Ni^{2+} superlattice at the sub-surface but also generate a 5 nm Li_2TiO_3 coating on the surface as well as a Ti doping in bulk. It should be emphasized that these multi-functional structural features are realized just by one-step calcination instead of a complex multi-step calcination process that has been widely taken in previous literature.

Regarding electrochemical performance, pristine NCMo90 shows initial discharge capacity of 216.3 mAh g^{-1} and coulombic efficiency of 89.2% at 0.1 C, respectively (Figure 3a). Comparatively, 1.0 mol% Ti-modified NCMo90

displays a slightly higher discharge capacity of 221 mAh g^{-1} and a comparable initial coulombic efficiency of 89.1%. Upon charge/discharge at 5 C (Figure 3b), 1.0 mol% Ti-modified NCMo90 displays a discharge capacity of 184.2 mAh g^{-1}, which is superior to pristine NCMo90 (175.0 mAh g^{-1}) and commercial NCMn90 (176.4 mAh g^{-1}) (Figure S13). In addition, the polarization of 1.0 mol% Ti-modified NCMo90 is significantly lower (Figure S14). The better rate capability is ascribed to the expanded Li–O lattice spacing caused by Ti-doping in the bulk and Li^+-conductive Li_2TiO_3 surface coating.[41,49,50] To further eval-
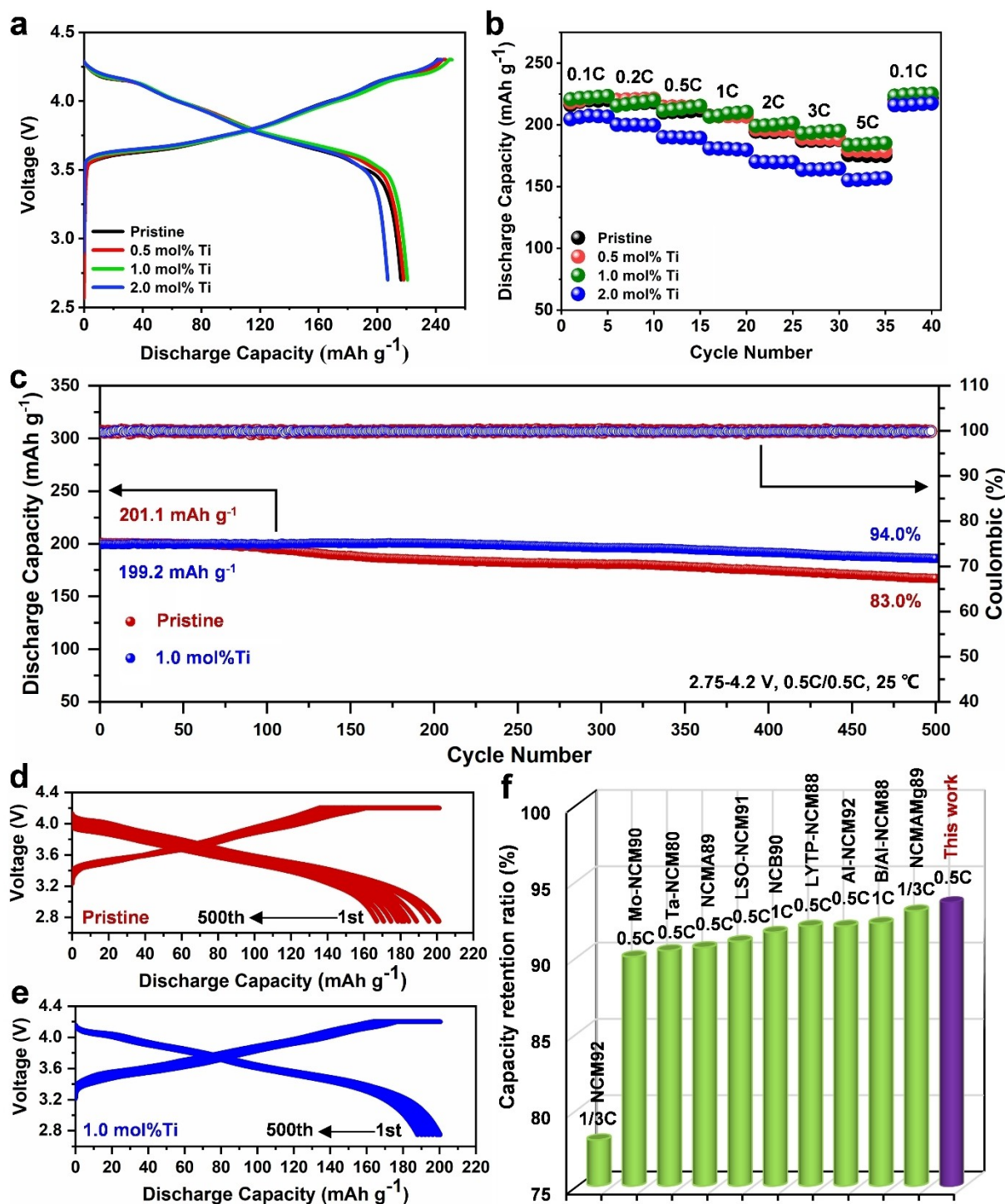
Figure 3. Electrochemical performances of pristine and modified NCMo90 with different amounts of Ti. (a) Initial charge–discharge curves at 0.1 C. (b) Rate performance from 0.1 C to 5 C. (c) Long-term cycling stability at 0.5 C of full-cells using graphite as the anodes and the corresponding charge–discharge curves of pristine (d) and 1.0 mol % Ti-modified NCMo90 (e). (f) Comparison of cycling stability of Ti-modified NCMo90 cathode with other Ni-rich cathodes after 100 cycles reported before.

uate the cycling stability, all the cathodes were further tested at 0.5 C and 1 C. As exhibited in Figure S15–S17, the 1.0 mol % Ti-modified cathode presents better cycling stability than pristine NCMo90 and commercial NCMn90. Meanwhile, the middle voltage of 1.0 mol % Ti-modified

NCMo90 is much more stable (Figure S18 and S19). To demonstrate the industrial applicability, the long-term cycling stability of 1.0 mol % Ti-modified NCMo90 cathode is verified in full cells that use graphite as the anode. The capacity retention of 1.0 mol % Ti-modified NCMo90 re-

mains at 94.0% after 500 cycles at 0.5 C, much higher than that of pristine NCMo90 (83.9%) (Figure 3c). Furthermore, 1.0 mol% Ti-modified NCMo90 displays excellent voltage profile stability compared to the pristine NCMo90 (Figures 3d and e). To the best of our knowledge, the cycling stability of 1.0 mol% Ti-modified NCMo90 demonstrated in this work outperforms all previous reports in the literature (Figure 3f and Table S3).

The dQ/dV profiles were obtained to compare the structural stability (Figure 4a and b). The reversible stepwise phase transition from H1 to H3 is detected in pristine and 1.0 mol% Ti-modified NCMo90. In comparison, 1.0 mol% Ti-modified NCMo90 is much more reversible, especially between H2 and H3. It is well documented that the phase transition between H2 and H3 may lead to significant contraction or expansion of the Li–O layer.[17,30,34] This abrupt change may result in intergranular cracking of cathode particles, eventually deteriorating cycling stability. The higher H2/H3 phase transition reversibility observed in 1.0 mol% Ti-modified NCMo90 explains its much-improved cycling stability.

In situ XRD was performed during the first charge process at 0.2 C to quantitatively assess the effect of the phase transition on the crystal structure (Figures 4c and d). The lattice parameters (a, c) and the unit cell volume (V) were calculated by fitting XRD spectra (Figures 4e, f and g). The (003) and (110) Bragg reflection peaks are related to the changes of the unit cell along the two different directions (c and a), respectively. The Bragg peak of (003) shifts to the low angle and then the high angle, which indicates the unit cell slowly expanding first along the c-direction and then contracting until the end of the charging. The variation (Δc) of lattice parameter c of 1.0 mol% Ti-modified NCMo90 is 3.51% (Figure 4e), considerably smaller than that of pristine NCMo90 (4.98%). Unlike the reflection peak of (003), the reflection peak of (110) continuously shifts to a high angle, suggesting the lattice parameter a gradually decreases upon delithiation. The variation (Δa) of lattice parameter a of 1.0 mol% Ti-modified NCMo90 is close to that of pristine NCMo90 (2.13% vs. 2.24%) (Figure 4f). Different from the variations in the lattice parameters a and c, the variation (ΔV) of unit cell volume of 1.0 mol% Ti-modified NCMo90 is significantly lower than that of pristine NCMo90 (5.39% vs. 7.65%) (Figure 4g). Based on previous reports,[51,52] the contraction of Li–O slabs along the c-direction is ascribed to the weakened pillar effect caused by considerable removal of Li$^+$ as well as reduced O–O coulombic repulsion force related to the charge transfer between O-2p and partially filled Ni-e$_g$ orbitals. The in situ XRD analysis corroborates that Ti-doping in bulk and coating on the surface can considerably reduce the anisotropic strain, thus maintaining the structural integrity of Ni-rich layered cathodes upon cycling.

To further illustrate the much-improved cycling stability of 1.0 mol% Ti-modified NCMo90, a post-mortem examination was performed on both electrodes after 100 cycles using SEM and TEM (Figure 5). Both pristine and Ti-modified secondary particles present microcracks (Figures 5a and 5b). Comparatively, 1.0 mol% Ti-modified NCMo90 exhibits significantly suppressed microcracks, which is consistent with the dQ/dV and in situ XRD results. This suggests that Ti doping in the bulk and Li$_2$TiO$_3$ coating on the surface can stabilize the H2–H3 phase transition and suppress microcracks. The well-aligned lattice of the pristine NCMo90 at the surface is distorted after 100 cycles (Figure 5c, region 1). The surface structure is changed to an Fm$\bar{3}$m phase related to nickel oxide (NiO) with a thickness of around 8 nm. By contrast, the NiO is only around 1 nm at the sub-surface of the Ti-modified NCMo90 (Figure 5d), demonstrating that Ti-modification can effectively suppress surface structural reconstruction from layered to rocksalt.

The interfacial NiO layer is electrochemically inactive and highly resistive, thus considerably affecting interfacial resistance.[32] We further conducted electrochemical impedance spectroscopy (EIS) analysis for the charged cathodes (4.3 V) to investigate the interfacial charge transfer kinetics (Figures S20a and S20b). Both cathodes present similar Nyquist plots, which can be assigned to four components in an equivalent circuit according to previous reports: ohmic resistance (R_s), surface film resistance (R_f), charge transfer resistance (R_{ct}), and the Warburg impedance (W_o).[38,43] The relationships between Z' and $\omega^{-1/2}$ were calculated based on impedance data to obtain the Warburg coefficient (Figures S20c and S20d). The reported equation, $D_{Li^+} = 0.5 R^2 T^2/(A^2 n^4 F^4 C^2 \sigma^2)$,[45] was used to calculate the Li$^+$ diffusion coefficients (D_{Li^+}), and the corresponding parameters are presented in Table S4. The Ti-modified NCMo90 exhibits a lower R_f and R_{ct} than the pristine one. Lower R_f implies fewer parasitic reactions and a thinner CEI, while lower R_{ct} indicates fast charge transfer. These advantages primarily result from the Li$_2$TiO$_3$ coating and Ti-doping. Therefore, the Ti-modified material shows a higher D_{Li^+} than the pristine one (9.48×10^{-11} vs. 6.34×10^{-11} cm^{2}s^{-1}) due to the enhanced Li$^+$ diffusion kinetics. As summarized in Table S4, the R_s and R_f for both cathodes have no apparent variations with cycling. It is worth noting that the R_{ct} for the pristine material remarkably increases from 22.22 to 1503 Ω, which implies the gradual formation and growth of inactive rocksalt phase on the surface confirmed by the HRTEM of cycled cathodes (Figure 5c). Comparatively, this value for the Ti-modified material shows a slight variation under the same condition, only increasing from 21.36 to 249.90 Ω. Importantly, the D_{Li^+} for both cathodes reduces to 2.43×10^{-12} cm^{2}s^{-1} and 7.41×10^{-14} cm^{2}s^{-1} after 100 cycles. These results indicate that Ti-modification can effectively prevent structural degradation and reduce the interfacial resistance of Ni-rich cathodes.

The detrimental parasitic reactions between electrolyte and cathode usually result in severe cycling degradation of cathodes. As determined by XPS, the surface chemical components of cycled materials can be used to evaluate the electrolyte decomposition on the cathode surface. The C1s and O1s spectra are mainly employed to evaluate the decomposition of carbonate solvent, while the F1s spectra are usually used to evaluate the decomposition of LiPF$_6$ salt.[26,43] As shown in Figure S21a, the feature peaks corresponding to the lithium alkyl carbonate or organic compounds can be observed in the C1s spectra for both
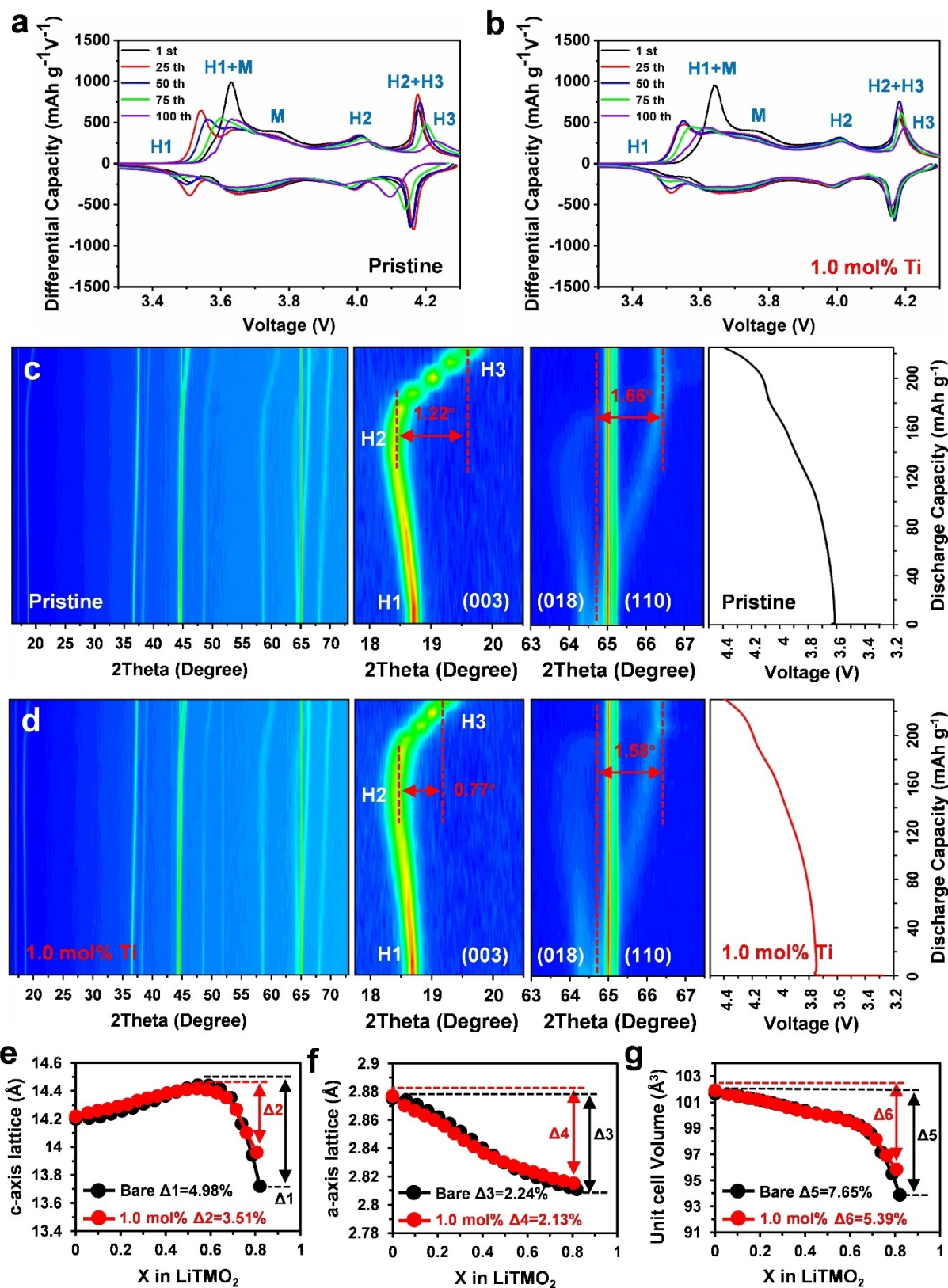
Figure 4. The d*Q*/d*V* profiles of pristine (a) and 1.0 mol% Ti-modified NCMo90 (b). (c) In situ XRD patterns of pristine NCMo90 and the corresponding charge curves from 3.0 to 4.4 V at 0.2 C. (d) In situ XRD patterns of 1.0 mol% Ti-modified NCMo90 and the corresponding charge curves from 3.0 to 4.4 V at 0.2 C. Variation of *c*-axis (e), *a*-axis (f) lattice parameters and unit cell volume (g) as a function of the extracted Li$^+$.
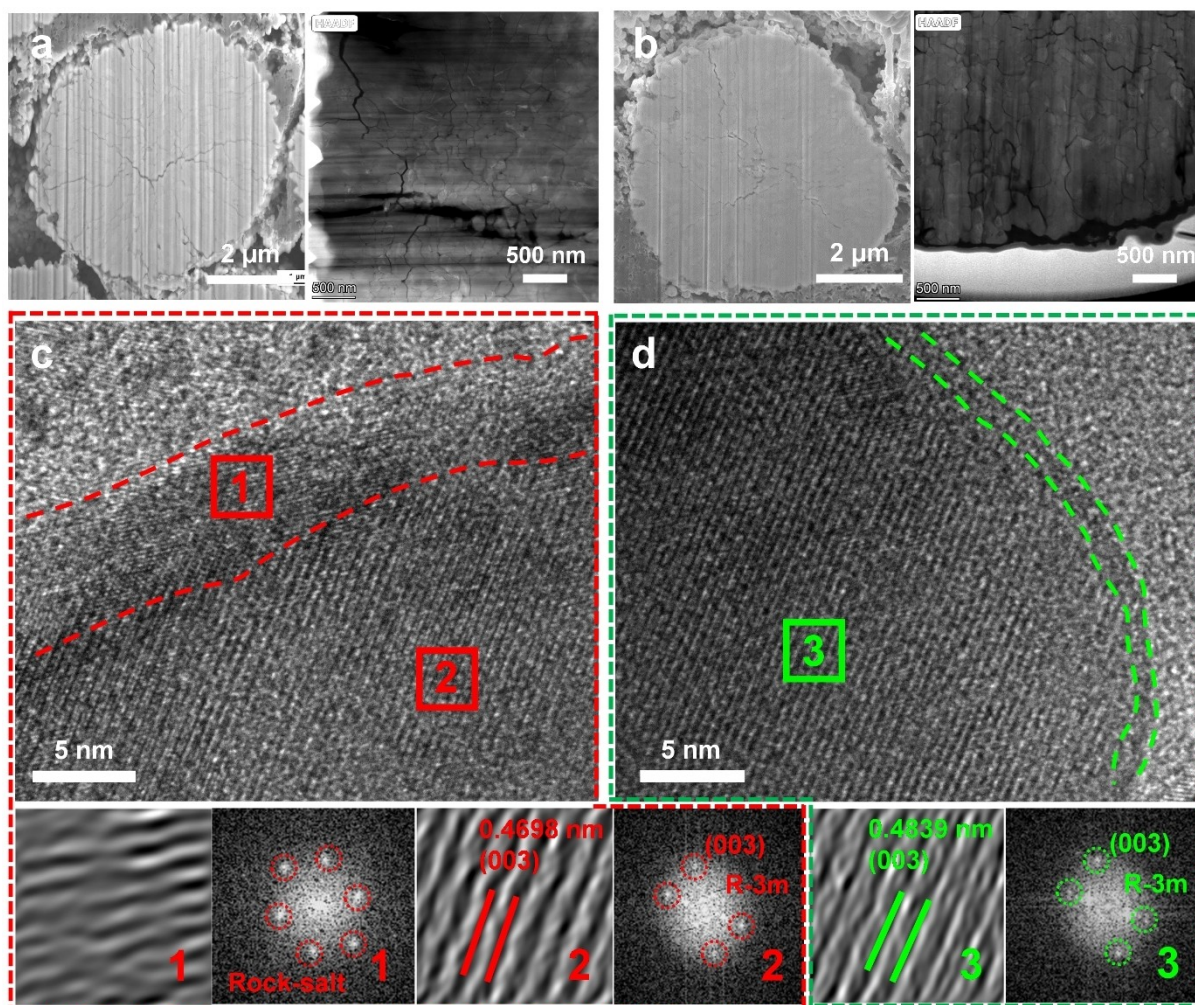
Figure 5. Cross-sectional SEM and Dark-field STEM images of pristine (a) and 1.0 mol % Ti-modified NCMo90 (b) after cycling at 1 C. High-resolution TEM image and the corresponding Fourier transforms from the marked regions of pristine (c) and 1.0 mol % Ti-modified NCMo90 (d) after cycling at 1 C.

cathodes. Moreover, the O 1s peaks related to Li_2CO_3 and $ROCO_2Li$ are also identified in the O 1s spectra for both cathodes (Figure S21b). However, the Ti-modified cathode presents weaker peak intensities than the pristine one, suggesting that the decomposition of carbonate solvent on the surface of the cathode can be suppressed by Ti-doping and Li_2TiO_3 coating.[22,26] Furthermore, other inorganic species, such as LiF, Li_xPF_y and $Li_xPO_yF_z$, are also observed by F 1s and P 2p spectra, which are typical decomposition products for electrolytes with $LiPF_6$ salt.[22,25,26] Compared to the pristine sample, the weaker peak intensities of F 1s and P 2p spectra for the Ti-modified NCMo90 (Figures S21c and S21d) also indicate the lower decomposition of $LiPF_6$ salt. These results consistently suggest that Li_2TiO_3 considerably suppresses electrolyte decomposition.

Conclusion

In this work, a bulk-doped, surface-coated Ni-rich NCMo90 cathode with a Li/TM cation-ordered superlattice at the sub-surface was successfully prepared by a first-of-its-kind coprecipitation and facile one-step calcination. Specifically, we take advantage of the diffusivity differences of Ti and Mo in layered cathodes, which leads to Ti partially diffusing into the bulk (with the remaining Ti being incorporated into a surface coating) while Mo only slightly doping the sub-surface and forming a Mo-rich Li/TM cation-ordered super-lattice. As a result, a multi-functional structure featuring a 5 nm Li_2TiO_3 coating on the surface, Ti-doping in the bulk, and a Mo-rich Li^+/Ni^{2+} cation-ordered superlattice at the sub-surface is simultaneously constructed in NCM90 during the one-step calcination process. These unique structural features have various functions in realizing the long-term cycling stability of NCM90: (1) the nanoscale surface coating can inhibit the interfacial electrolyte decomposition and HF attacks; (2) Ti doping in bulk can increase the Li–O slab

heights, strengthen metal-oxygen bonds and improve the electronic conductivity; and (3) the Mo-rich Li/TM cation-ordered superlattice at the sub-surface can effectively suppress the surface structural reconstruction from layered structure to rocksalt phase. As a result, such unique NCMo90 demonstrates a high discharge capacity of 221 mAh g^{-1} at 0.1 C, good rate performance (184 mAh g^{-1} at 5 C), and high capacity retention of 94.0 % after 500 cycles. Our innovative synthesis strategy may be applicable to other cathodes, providing a new avenue for developing next-generation LIBs with lower cost, longer cycling stability, and higher energy density.

Conflict of Interest

The authors declare no conflict of interest.

Data Availability Statement

The data that support the findings of this study are available from the corresponding author upon reasonable request.

Keywords: Bulk-to-Surface Modification · Li-Ion Batteries · Ni-Rich Cathodes · One-Step Synthesis · Ordered Superlattice

[1] W. D. Li, E. M. Erickson, A. Manthiram, *Nat. Energy* **2020**, *5*, 26–34.

[2] H. H. Ryu, H. H. Sun, S. T. Myung, C. S. Yoon, Y. K. Sun, *Energy Environ. Sci.* **2021**, *14*, 844–852.

[3] K. Y. Zhang, Z. Y. Gu, E. H. Ang, J. Z. Guo, X. T. Wang, Y. L. Wang, X. L. Wu, *Mater. Today* **2022**, *54*, 189–201.

[4] X. X. Wang, Y. L. Ding, Y. P. Deng, Z. W. Chen, *Adv. Energy Mater.* **2020**, *10*, 1903864.

[5] J. U. Choi, N. Voronina, Y. K. Sun, S. T. Myung, *Adv. Energy Mater.* **2020**, *10*, 2002027.

[6] F. Lin, I. M. Markus, D. Nordlund, T. C. Weng, M. D. Asta, H. L. Xin, M. M. Doeff, *Nat. Commun.* **2014**, *5*, 3529.

[7] H. H. Ryu, K. J. Park, C. S. Yoon, Y. K. Sun, *Chem. Mater.* **2018**, *30*, 1155–1163.

[8] D. S. Ko, J. H. Park, B. Y. Yu, D. Ahn, K. Kim, H. N. Han, W. S. Jeon, C. H. A. Jung, *Adv. Energy Mater.* **2020**, *10*, 2001035.

[9] G. W. Nam, N. Y. Park, K. J. Park, J. H. Yang, J. Liu, C. S. Yoon, Y. K. Sun, *ACS Energy Lett.* **2019**, *4*, 2995–3001.

[10] S. Y. Lee, G. S. Park, C. H. Jung, D. S. Ko, S. Y. Park, H. G. Kim, S. H. Hong, Y. M. Zhu, M. Y. Kim, *Adv. Sci.* **2019**, *6*, 1800843.

[11] J. H. Kim, H. H. Ryu, S. J. Kim, C. S. Yoon, Y. K. Sun, *ACS Appl. Mater. Interfaces* **2019**, *11*, 30936–30942.

[12] K. J. Park, J. Y. Hwang, H. H. Ryu, F. Maglia, S. J. Kim, P. Lamp, C. S. Yoon, Y. K. Sun, *ACS Energy Lett.* **2019**, *4*, 1394–1400.

[13] X. Xu, H. Huo, J. Y. Jian, L. G. Wang, H. Zhu, S. Xu, X. S. He, G. P. Yin, C. Y. Du, X. L. Sun, *Adv. Energy Mater.* **2019**, *9*, 1803963.

[14] F. Wu, N. Liu, L. Chen, Y. F. Su, Y. Lu, J. Wang, S. Chen, J. Tan, *Nano Energy* **2019**, *59*, 50–57.

[15] F. Xia, D. Tie, J. Wang, H. L. Song, W. Wen, X. X. Ye, J. S. Wu, Y. L. Hou, X. G. Lu, Y. F. Zhao, *Energy Storage Mater.* **2021**, *42*, 209–218.

[16] H. H. Ryu, N. Y. Park, J. H. Seo, Y. S. Yu, M. Sharma, R. Mücke, P. Kaghazchi, C. S. Yoon, Y. K. Sun, *Mater. Today* **2020**, *36*, 73–82.

[17] H. H. Ryu, N. Y. Park, D. R. Yoon, U. H. Kim, C. S. Yoon, Y. K. Sun, *Adv. Energy Mater.* **2020**, *10*, 2000495.

[18] C. H. Jung, D. H. Kim, D. Eum, K. H. Kim, J. Choi, J. Lee, H. H. Kim, K. Kang, S. H. Hong, *Adv. Funct. Mater.* **2021**, *31*, 2010095.

[19] N. Y. Park, H. H. Ryu, L. Y. Kuo, P. Kaghazchi, C. S. Yoon, Y. K. Sun, *ACS Energy Lett.* **2021**, *6*, 4195–4202.

[20] Q. H. Shi, R. J. Qi, X. C. Feng, J. Wang, Y. Li, Z. P. Yao, X. Wang, Q. Q. Li, X. G. Lu, J. J. Zhang, Y. F. Zhao, *Nat. Commun.* **2022**, *13*, 3205.

[21] Z. Y. Gu, J. Z. Guo, Z. H. Sun, X. X. Zhao, X. T. Wang, H. J. Liang, X. L. Wu, Y. C. Liu, *Cell Rep. Phys. Sci.* **2021**, *2*, 100665.

[22] M. Yoon, Y. Dong, J. Y. Hwang, J. Sung, H. Cha, K. Ahn, Y. M. Huang, S. J. Kang, J. Li, J. Cho, *Nat. Energy* **2021**, *6*, 362–371.

[23] W. M. Seong, K. H. Cho, J. W. Park, H. Park, D. Eum, M. H. Lee, I. S. Kim, J. Lim, K. Kang, *Angew. Chem. Int. Ed.* **2020**, *59*, 18662–18669.

[24] H. F. Yu, Y. P. Cao, L. Chen, Y. J. Hu, X. Z. Duan, S. Dai, C. Z. Li, H. Jiang, *Nat. Commun.* **2021**, *12*, 4564.

[25] Y. J. Sun, W. J. Huang, G. F. Zhao, Q. Liu, L. Y. Duan, S. M. Wang, Q. An, H. Wang, Y. X. Yang, C. H. Zhang, H. Guo, *ACS Energy Lett.* **2023**, *8*, 1629–1638.

[26] X. M. Fan, X. Ou, W. G. Zhao, Y. Liu, B. Zhang, J. F. Zhang, L. F. Zou, L. Seidl, Y. Z. Li, G. R. Hu, C. Battaglia, Y. Yang, *Nat. Commun.* **2021**, *12*, 5320.

[27] U. H. Kim, H. H. Ryu, J. H. Kim, R. Mücke, P. Kaghazchi, C. S. Yoon, Y. K. Sun, *Adv. Energy Mater.* **2019**, *9*, 1803902.

[28] U. H. Kim, J. H. Kim, J. Y. Hwang, H. H. Ryu, C. S. Yoon, Y. K. Sun, *Mater. Today* **2019**, *23*, 26–36.

[29] H. H. Ryu, N. Y. Park, T. C. Noh, G. C. Kang, F. Maglia, S. J. Kim, C. S. Yoon, Y. K. Sun, *ACS Energy Lett.* **2020**, *5*, 216–223.

[30] G. T. Park, N. Y. Park, T. C. Noh, B. Namkoong, H. H. Ryu, J. Y. Shin, T. Beierling, C. S. Yoon, Y. K. Sun, *Energy Environ. Sci.* **2021**, *14*, 5084–5095.

[31] N. Y. Park, H. H. Ryu, G. T. Park, T. C. Noh, Y. K. Sun, *Adv. Energy Mater.* **2021**, *11*, 2003767.

[32] G. T. Park, H. H. Ryu, N. Y. Park, C. S. Yoon, Y. K. Sun, *J. Power Sources* **2019**, *442*, 227242.

[33] U. H. Kim, N. Y. Park, G. T. Park, H. G. Kim, C. S. Yoon, Y. K. Sun, *Energy Storage Mater.* **2020**, *33*, 399–407.

[34] H. H. Ryu, K. J. Park, D. R. Yoon, A. Aishova, C. S. Yoon, Y. K. Sun, *Adv. Energy Mater.* **2019**, *9*, 1902698.

[35] U. H. Kim, G. T. Park, B. K. Son, G. W. Nam, J. Liu, L. Y. Kuo, P. Kaghazchi, C. S. Yoon, Y. K. Sun, *Nat. Energy* **2020**, *5*, 860–869.

[36] H. H. Sun, U. H. Kim, J. H. Park, S. W. Park, D. H. Seo, A. Heller, C. B. Mullins, C. S. Yoon, Y. K. Sun, *Nat. Commun.* **2021**, *12*, 6552.

[37] Y. J. Guo, C. H. Zhang, S. Xin, J. L. Shi, W. P. Wang, M. Fan, Y. X. Chang, W. H. He, E. H. Wang, Y. G. Zou, X. A. Yang, F. Q. Meng, Y. Y. Zhang, Z. Q. Lei, Y. X. Yin, Y. G. Guo, *Angew. Chem. Int. Ed.* **2022**, *61*, e202116865.

[38] H. P. Yang, H. H. Wu, M. Y. Ge, L. J. Li, Y. F. Yuan, Q. Yao, J. Chen, L. F. Xia, J. M. Zheng, Z. Y. Chen, J. F. Duan, K. Kisslinger, X. C. Zeng, W. K. Lee, Q. B. Zhang, J. Lu, *Adv. Funct. Mater.* **2019**, *29*, 1808825.

[39] J. Lu, Q. Peng, W. Y. Wang, C. Y. Nan, L. H. Li, Y. D. Li, *J. Am. Chem. Soc.* **2013**, *135*, 1649–1652.

[40] K. Meng, Z. X. Wang, H. J. Guo, X. H. Li, D. Wang, *Electrochim. Acta* **2016**, *211*, 822–831.

[41] F. Xiong, Z. X. Chen, C. Huang, T. Z. Wang, W. X. Zhang, Z. H. Yang, F. Chen, *Inorg. Chem.* **2019**, *58*, 15498–15506.

[42] E. Y. Zhao, X. F. Liu, Z. B. Hu, L. M. Sun, X. L. Xiao, *J. Power Sources* **2015**, *294*, 141–149.

[43] G. C. Yang, K. Pan, F. Y. Lai, Z. M. Wang, Y. Q. Chu, S. L. Yang, J. L. Han, H. Q. Wang, X. H. Zhang, Q. Y. Li, *Chem. Eng. J.* **2021**, *421*, 129964.

[44] Y. Yang, S. M. Xu, M. Xie, Y. H. He, G. Y. Huang, Y. C. Yang, *J. Alloys Compd.* **2015**, *619*, 846–853.

[45] Y. J. Sun, Z. D. Liu, X. C. Chen, X. P. Yang, F. W. Xiang, W. Lu, *Electrochim. Acta* **2021**, *376*, 138038.

[46] Q. Q. Qiu, Z. Shadike, Q. C. Wang, X. Y. Yue, X. L. Li, S. S. Yuan, F. Fang, X. J. Wu, A. Hunt, I. Waluyo, S. M. Bak, X. Q. Yang, Y. N. Zhou, *ACS Appl. Mater. Interfaces* **2019**, *11*, 23213–23221.

[47] X. S. He, X. Xu, L. G. Wang, C. Y. Du, X. Q. Cheng, P. J. Zuo, Y. L. Ma, G. P. Yin, *J. Electrochem. Soc.* **2019**, *166*, A143–A150.

[48] G. T. Park, B. Namkoong, S. B. Kim, J. Liu, C. S. Yoon, Y. K. Sun, *Nat. Energy* **2022**, *7*, 946–954.

[49] I. M. Markus, F. Lin, K. C. Kam, M. Asta, M. M. Doeff, *J. Phys. Chem. Lett.* **2014**, *5*, 3649–3655.

[50] D. F. Kong, J. T. Hu, Z. F. Chen, K. P. Song, C. Li, M. Y. Weng, M. F. Li, R. Wang, T. C. Liu, J. J. Liu, M. J. Zhang, Y. G. Xiao, F. Pan, *Adv. Energy Mater.* **2019**, *9*, 1901756.

[51] A. O. Kondrakov, H. Geßwein, K. Galdina, L. D. Biasi, V. Meded, E. O. Filatova, G. Schumacher, W. Wenzel, P. Hartmann, T. Brezesinski, J. Janek, *J. Phys. Chem. C* **2017**, *121*, 24381–24388.

[52] A. O. Kondrakov, A. Schmidt, J. Xu, H. Geßwein, R. Mönig, P. Hartmann, H. Sommer, T. Brezesinski, J. Janek, *J. Phys. Chem. C* **2017**, *121*, 3286–3294.